Electronic Supplementary Information for

Luminous Efficiency Roll-Off Mechanism in $CsPbBr_{3-x}Cl_x$ Mixed-Halide Perovskite Quantum Dot Blue Light-Emitting Diodes

Young Ran Park,[a] Hong Hee Kim,[b] Sangwon Eom,[c] Won Kook Choi,[b] Hyosung Choi,[c] Bo Ram Lee,[d] and Youngjong Kang*[a,c]

[a] Institute of Nano Science and Technology (INST), Hanyang University, Seongdong-gu, Seoul 04763, Korea
[b] Center for Opto-Electronic Materials and Devices, Korea Institute of Science and Technology (KIST), Seongbuk-gu, Seoul 02792, Korea
[c] Department of Chemistry, Hanyang University, Seongdong-gu, Seoul 04763, Korea
[d] Department of Physics, Pukyong National University, Busan 48513, Korea

*Correspondence and requests for materials should be addressed to Y.K. (E-mail: youngjkang@hanyang.ac.kr)

This file includes:

Supplementary Figures 1–9;

Supplementary table S1;

Supplementary Descriptions;

Supplementary References

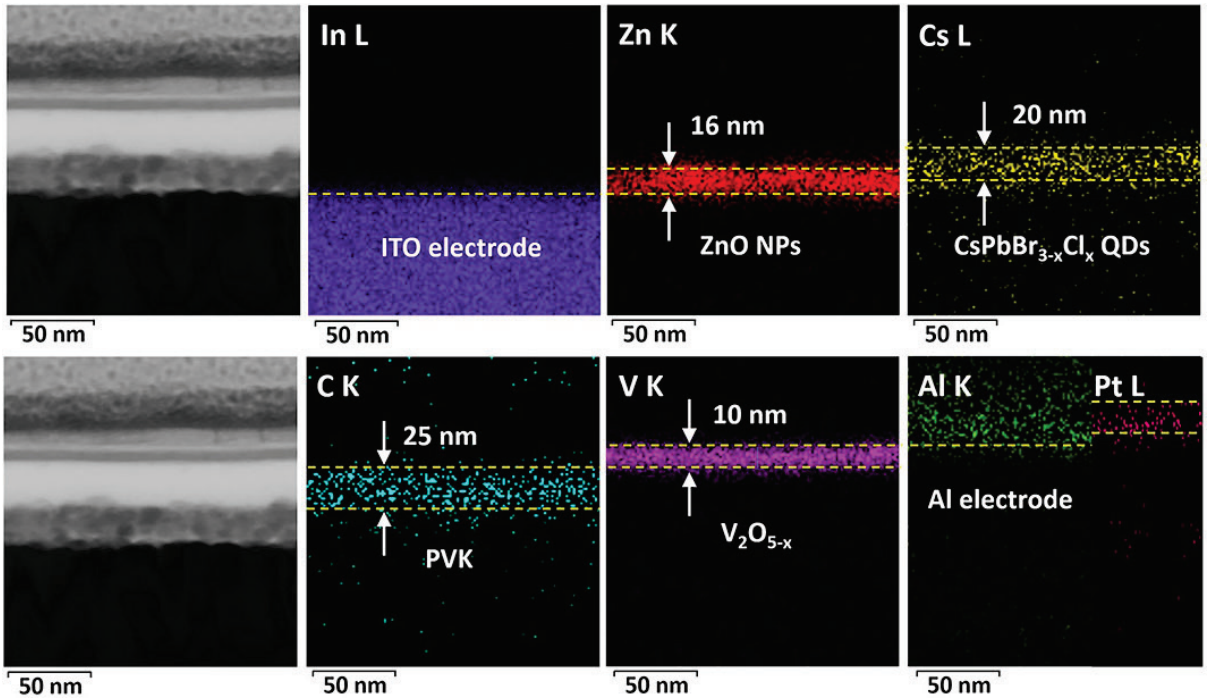

Fig. S1. Cross-sectional TEM (leftmost) and the corresponding EDX mapping images for elements of In, Zn, Cs, C, V, and Al (from left to right).

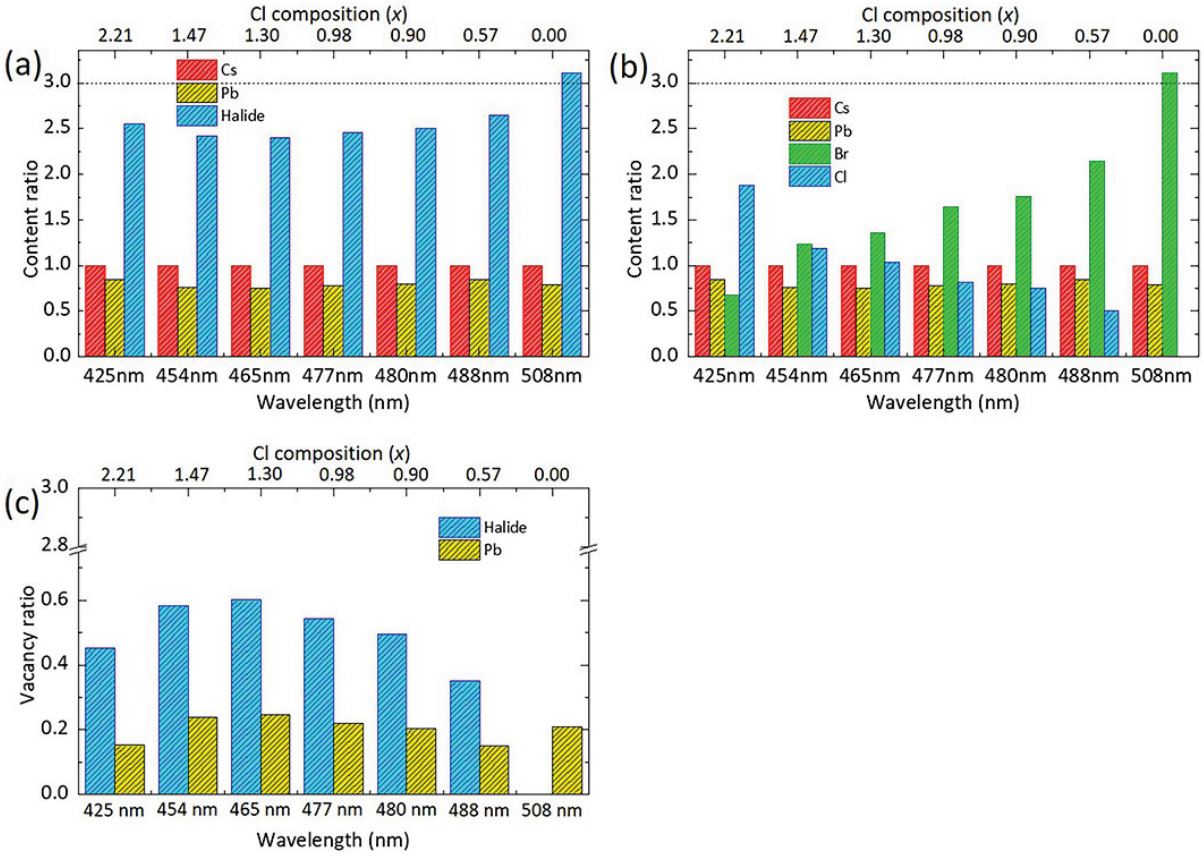

Fig. S2. (a-b) Elemental ratio and (c) halide (V_{halide}) and Pb vacancy (V_{Pb}) in $CsPbBr_{3-x}Cl_x$ QDs determined by XPS (Fig. S5) and STEM-EDX (Fig. S6). (a) The changes of Cs, Pb, and halide, ratio, and (b) Cs, Pb, Br, and Cl with varying the Cl composition ($0 \leq x \leq 2.21$). (c) The changes of halide (V_{halide}) and Pb vacancy (V_{Pb}) ratio in $CsPbBr_{3-x}Cl_x$ QDs as a function of the Cl composition ($0 \leq x \leq 2.21$).

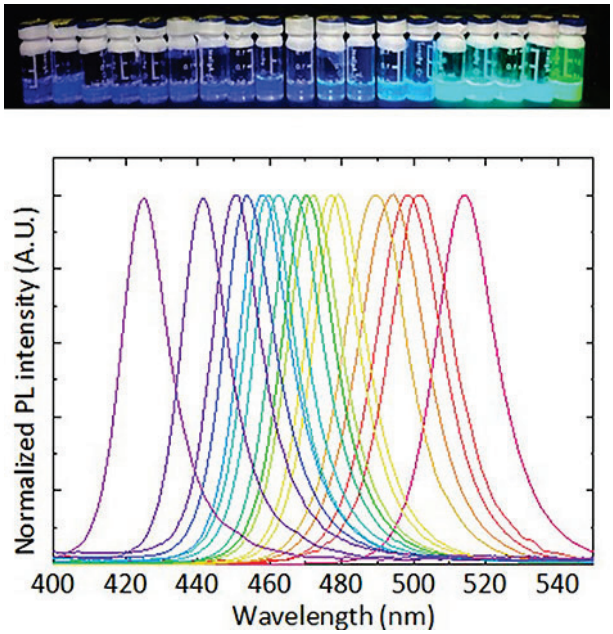

Fig. S3. The photograph of the colloidal solutions of $CsPbBr_{3-x}Cl_x$ QDs under UV-light excitation, λ=365 nm (upper panel). Representative PL spectra of $CsPbBr_{3-x}Cl_x$ QDs (lower panel).

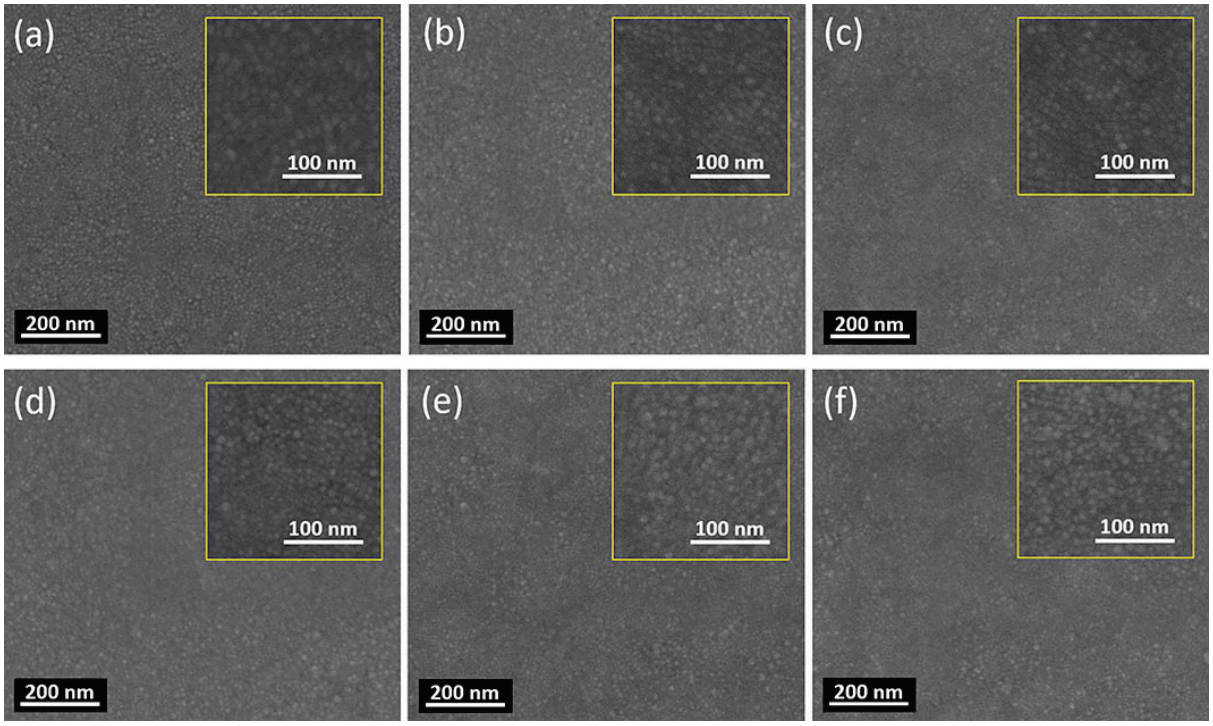

Fig. S4. Surface analyses of $CsPbBr_{3-x}Cl_x$ QD films on *b*-PEI/ZnO/ITO obtained by FE-SEM. (a) x = 0.57, (b) x = 0.90, (c) x = 0.98, (d) x = 1.30, (e) x = 1.47, and (f) x = 2.21.

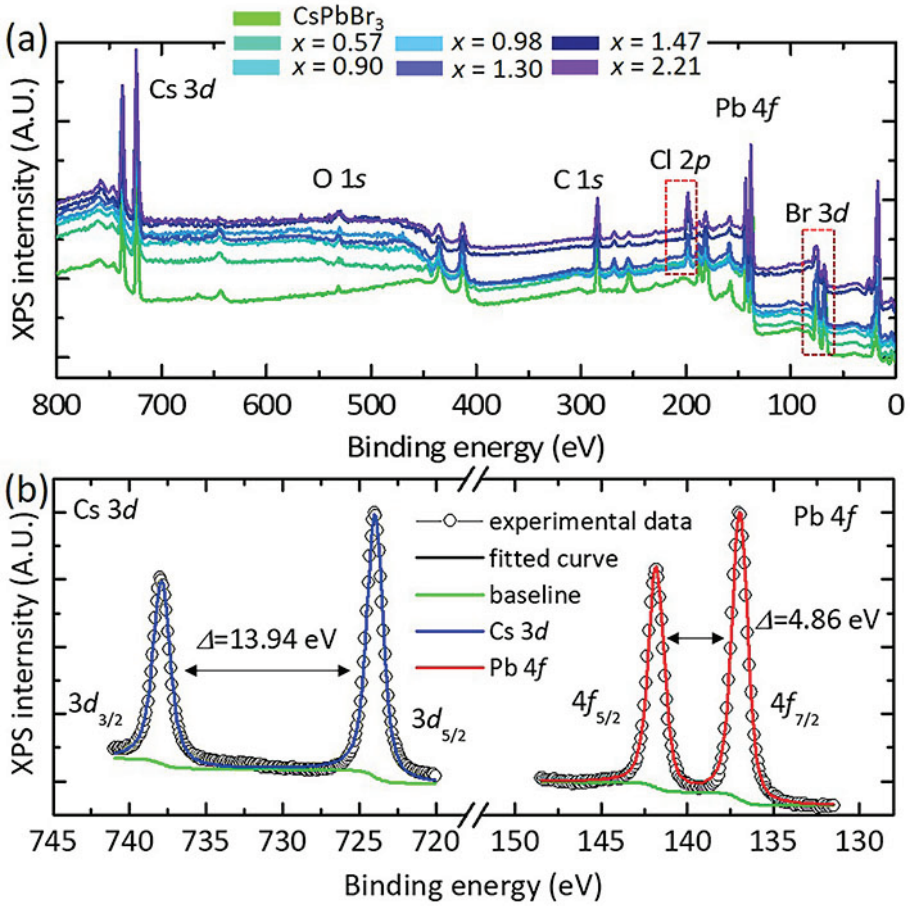

Fig. S5. XPS analyses of $CsPbBr_{3-x}Cl_x$ QDs. (a) XPS survey spectra showing Br 3*d*, Pb 4*f*, Cl 2*p*, C 1*s*, N 1*s*, O 1*s*, and Cs 3*d*. (b) High-resolution XPS data for Cs 3*d* and Pb 4*f*. No metallic Pb^0 peak was observed.

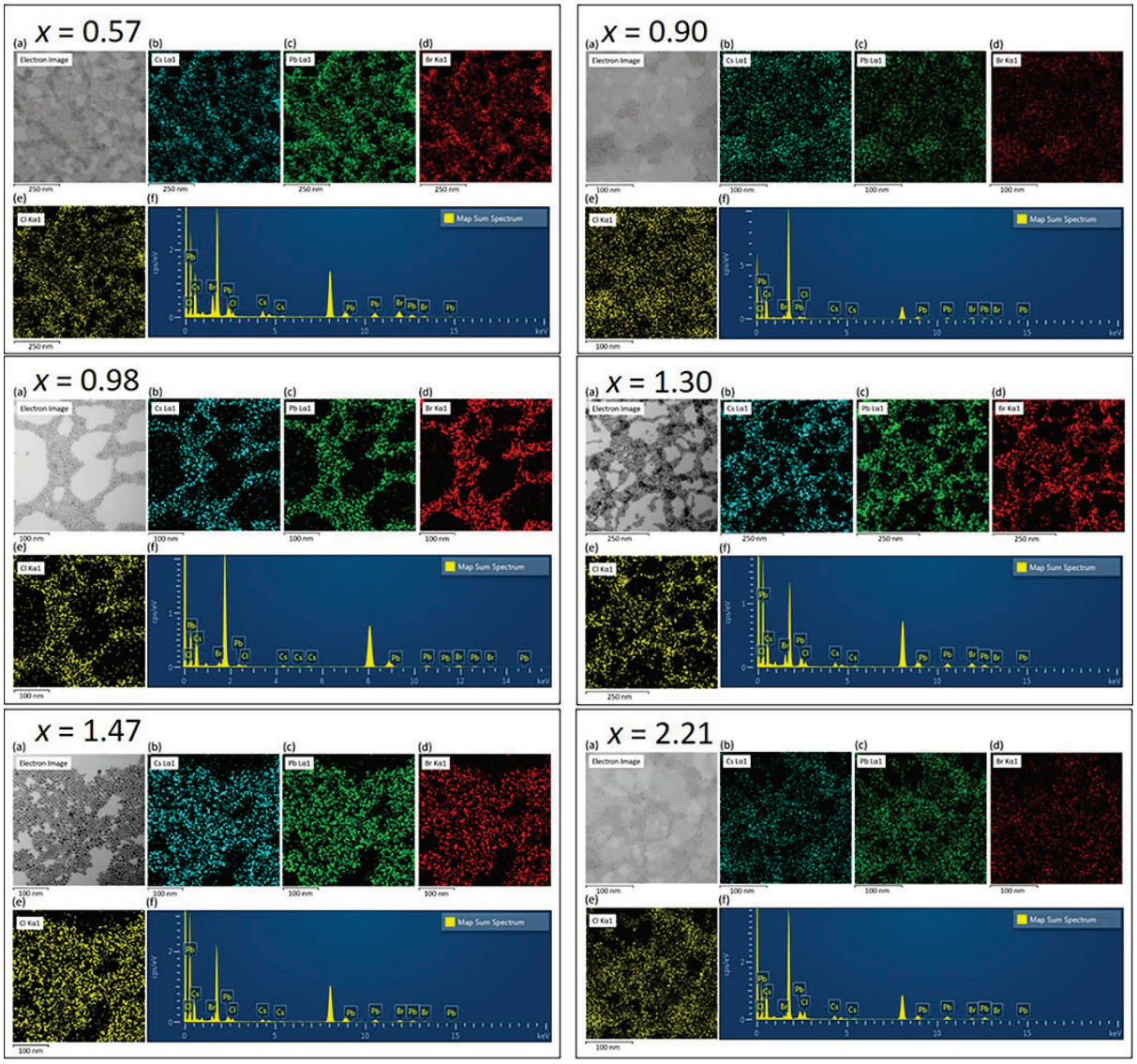

Fig. S6. STEM-EDX mapping of $CsPbBr_{3-x}Cl_x$ QDs. (a) Bright-field STEM micrograph of $CsPbBr_{3-x}Cl_x$ QDs. (b-e) The corresponding EDX mapping of $CsPbBr_{3-x}Cl_x$ QDs: (b) Cs (cyan), (c) Pb (green), (d) Br (red), and (e) Cl (yellow). (f) STEM-EDX spectra of $CsPbBr_{3-x}Cl_x$ QDs.

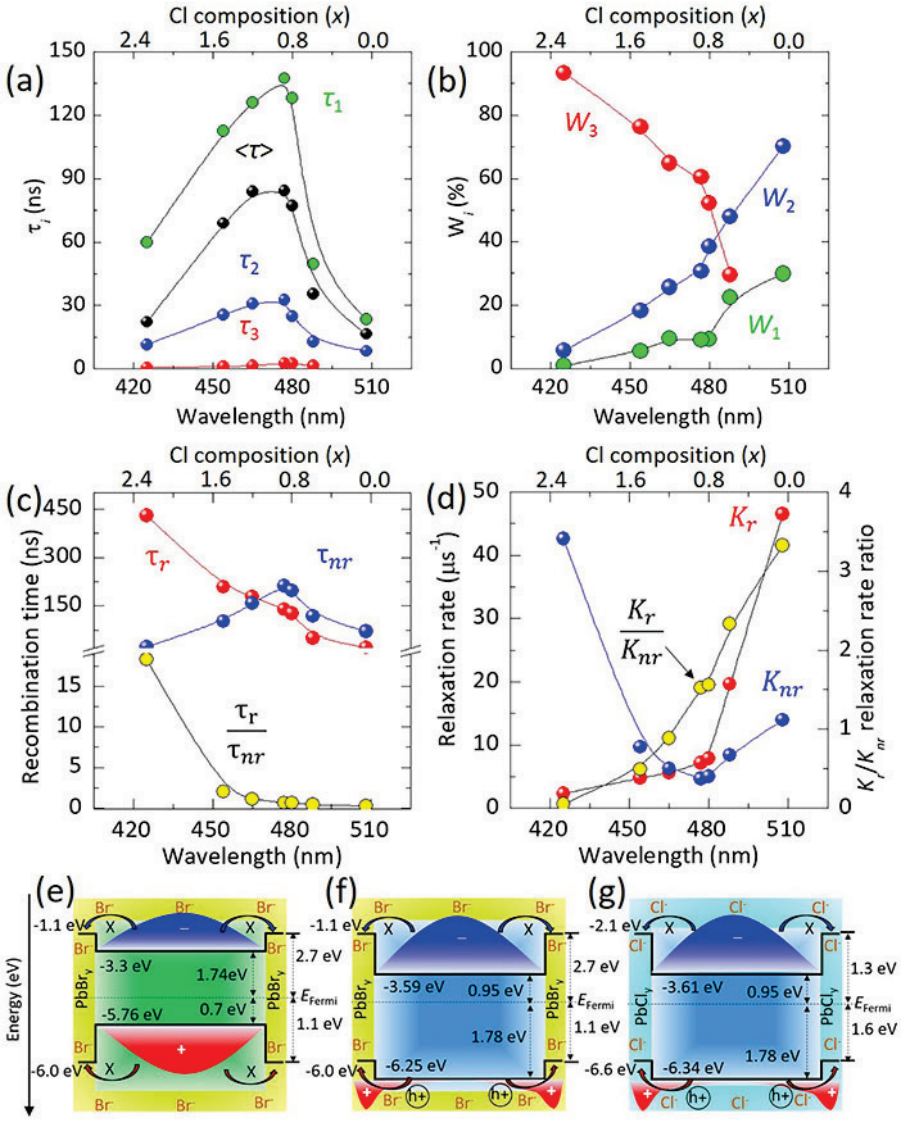

Fig. S7. Time-resolved PL spectra for $CsPbBr_{3-x}Cl_x$ QDs. (a) decay time τ_i and average tim <τ> and (b) amplitude W_i by using tri-exponential model fitting process. (c) Radiative (τ_r) recombination lifetime, nonradiative (τ_{nr}) recombination lifetime, and radiative (τ_r)/nonradiative (τ_{nr}) recombination lifetime ratio and (d) radiative (K_r) relaxation rate, nonradiative (K_{nr}) relaxation rate, and radiative (K_r)/nonradiative (K_{nr}) relaxation rate ratio for $CsPbBr_{3-x}Cl_x$ QDs. Schematic diagram of the Br rich surface and assumed energy levels within the QDs. Energy level diagrams and charge wave functions of the proposed (e) type I core/shell ($CsPbBr_3/PbBr_y$), (f) inverse type II core/shell ($CsPbBr_{3-x}Cl_x$(type E)/$PbBr_y$), and (g) inverse type II core/shell ($CsPbBr_{3-x}Cl_x$(x = 1.47)/$PbCl_y$).

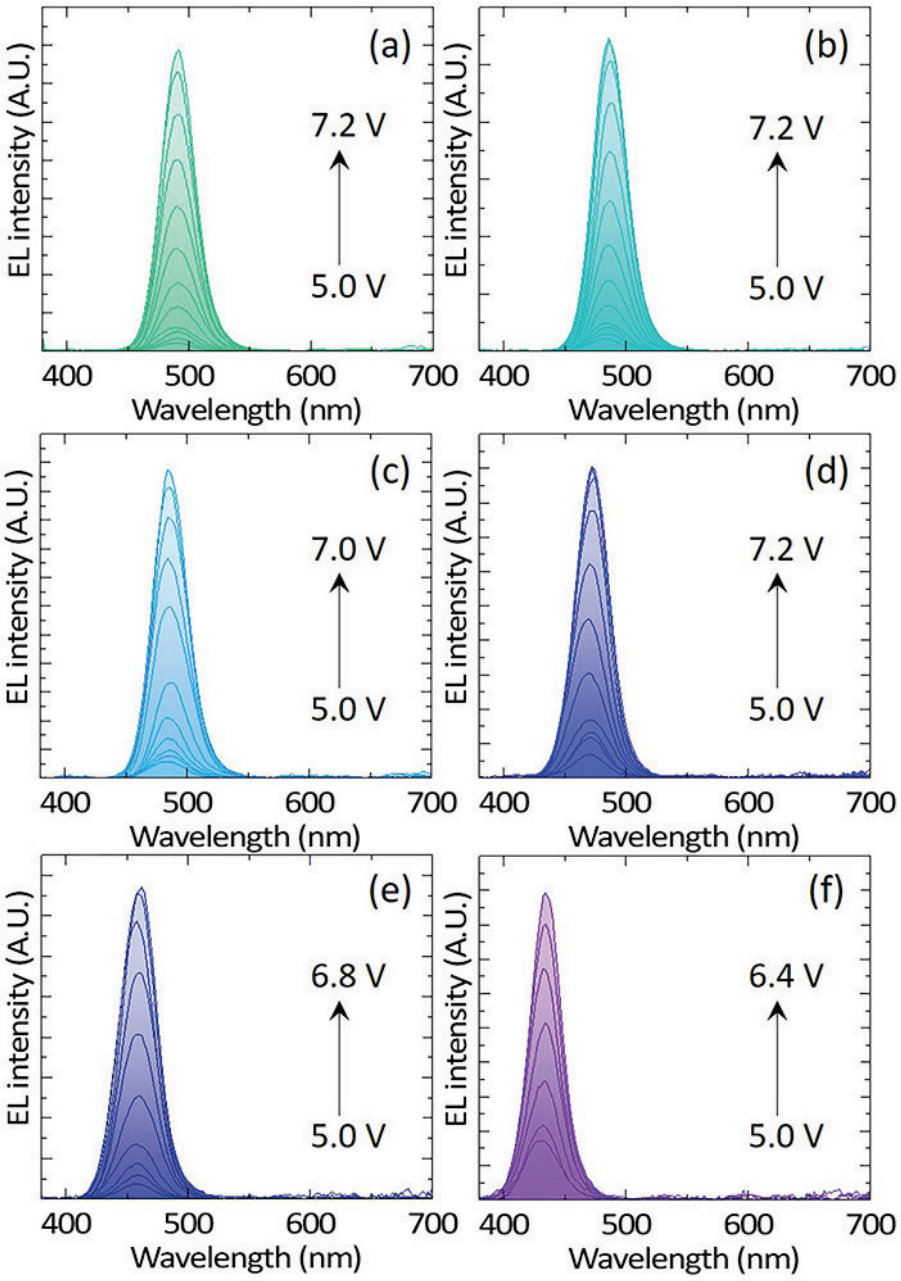

Fig. S8. EL spectra of $CsPbBr_{3-x}Cl_x$ QD-LEDs at diverse applied voltages. (a) x = 0.57, (b) x = 0.90, (c) x = 0.98, (d) x = 1.30, (e) x = 1.47, and (f) x = 2.21.

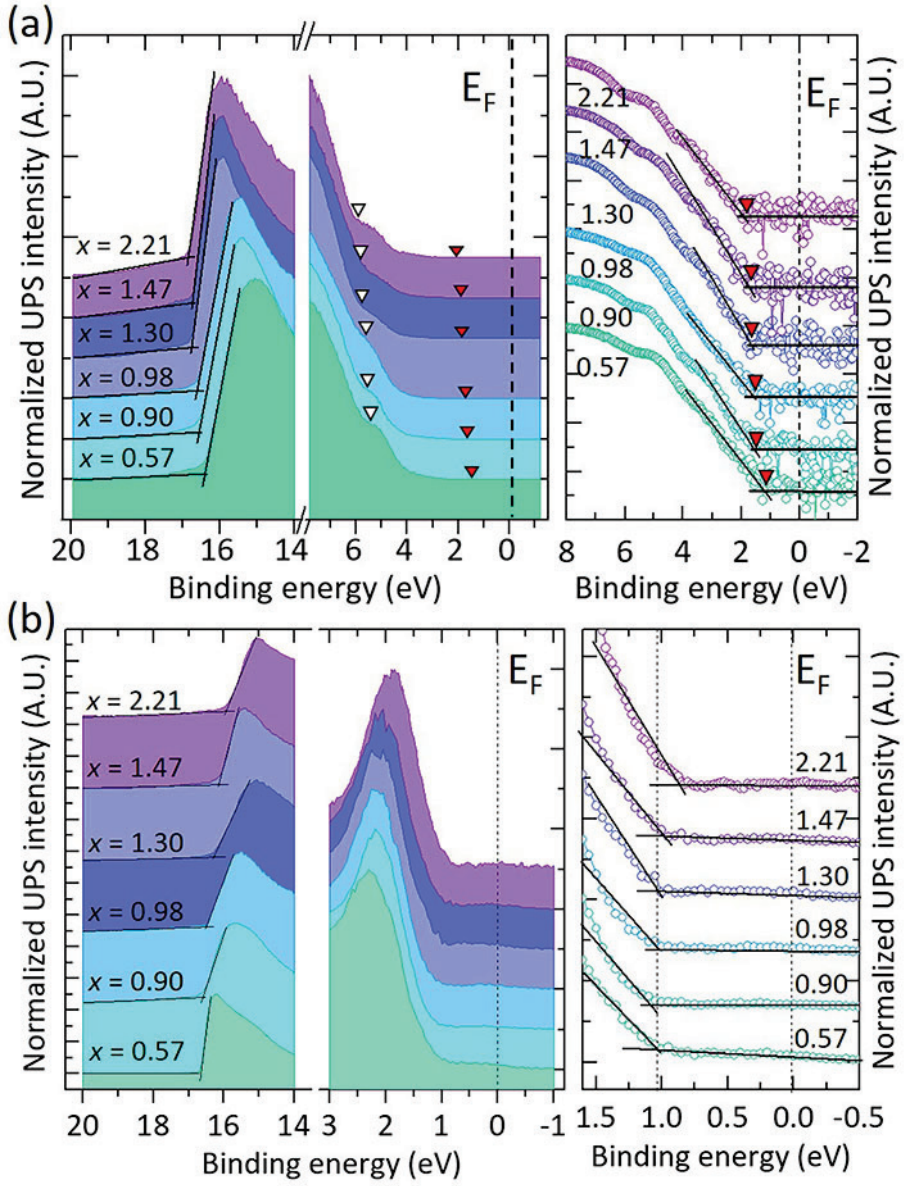

Fig. S9. UPS data of multilayer heterojunctions recorded (Left) in the low kinetic energy region (the secondary electron cutoff), and (right) in the low-binding-energy region (VBM region). (a) $CsPbBr_{3-x}Cl_x$ on *b*-PEI/ZnO/ITO and (b) PVK on $CsPbBr_{3-x}Cl_x$/*b*-PEI/ZnO/ITO.

Table S1. Summary of the time-resolved PL decay profiles[a] of $CsPbBr_{3-x}Cl_x$ QDs with varying the Cl composition (x)

x	0.00[1]	0.57	0.90	0.98	1.30	1.47	2.21
PL peak[b] (nm)	508	488	480	477	465	454	425
A	26.3_1	6.7_8	12.4_3	16.1_1	18.4_5	11.4_7	4.6_3
W_1 (%)	70.0_9	22.4_7	9.3_1	8.8_9	9.5_2	5.3_9	0.9_4
τ_1 (ns)	8.4_7	49.6_0	128.0_4	137.4_5	125.9_7	112.6_2	59.7_6
W_2 (%)	29.9_1	47.9_5	38.5_5	30.6_7	25.6_6	18.3_0	5.7_9
τ_2 (ns)	23.3_7	12.9_9	25.0_4	32.6_9	31.0_0	25.5_0	11.5_5
W_3 (%)	-	29.5_8	52.1_4	60.4_4	64.8_3	76.3_0	93.2_7
τ_3 (ns)	-	1.4_7	2.5_5	2.6_5	1.5_1	1.1_6	0.6_9
τ_{avg} (ns)	16.5_3	35.6_0	77.3_0	84.3_6	84.0_4	68.9_1	22.2_6
τ_r (ns)	21.5_1	50.8_6	126.8_9	139.7_4	179.1_0	208.2_9	429.7_6
τ_{nr} (ns)	71.4_3	118.6_7	197.8_0	212.8_7	158.3_4	102.9_8	23.4_8
τ_r/τ_{nr}	0.3_0	0.4_3	0.6_4	0.6_6	1.1_3	2.0_2	18.3_1
K_r (μs^{-1})	46.5_0	19.6_6	7.8_8	7.1_6	5.5_8	4.8_0	2.3_3
K_{nr} (μs^{-1})	14.0_0	8.4_3	5.05_6	4.7_0	6.3_2	9.7_1	42.5_9
K_r/K_{nr}	3.3_2	2.3_3	1.5_6	1.5_2	0.8_8	0.4_3	0.0_5

[a] The PL decay curves were numerically analyzed using a tri-exponential model fitting expressed by

$$I(t) = A + W_1 e^{(-\frac{t}{\tau_1})} + W_2 e^{(-\frac{t}{\tau_2})} + W_3 e^{(-\frac{t}{\tau_3})},$$

where I, t, W, and τ is normalized emission intensity, time after excitation, amplitude coefficient, and decay time constant, respectively.

[b] In a solution

Supplementary References

1. Y. R. Park, S. Eom, H. H. Kim, W. K. Choi and Y. Kang, *Sci Rep*, 2020, **10**, 14758.